GEOPHYSICS, VOL. 79, NO. 4 (JULY-AUGUST 2014); P. T189–T197, 15 FIGS.
10.1190/GEO2014-0012.1

An accuracy analysis of a Hamiltonian particle method with the staggered particles for seismic-wave modeling including surface topography

Junichi Takekawa[1], Hitoshi Mikada[1], and Tada-nori Goto[1]

ABSTRACT

A Hamiltonian particle method (HPM), which is one of the mesh-free methods, can simulate seismic wavefields for models including surface topography in a simple manner. Numerical error caused by a curved free surface or by particles not aligned with the surface is not obvious in HPM. In general, the accommodation of irregular free surfaces requires more grids or particles in a minimum wavelength for achieving sufficient accuracy in the simulation. We tested the accuracy of HPM with staggered particles for simulating seismic-wave propagation including the surface topography, and we established the relationship between desired accuracy and spatial resolution. We conducted numerical simulations for models with a planar free surface aligned with the regular particle alignment and a dipping free surface. Our accuracy tests revealed that the numerical error strongly depends on the dipping angle of the slope. We concluded that about 25 particles in a minimum wavelength are required to calculate Rayleigh waves propagating along the irregular topography with good accuracy. Finally, we simulated Rayleigh wave propagation along irregular topography using a layered model with a hill. HPM can reproduce not only surface-wave propagation but also the reflected and refracted waves. Our numerical results were in good agreement with those from a finite-element method. Our investigations indicated that HPM could be a solution to simulate Rayleigh waves in the presence of complex surface topography.

INTRODUCTION

Numerical simulations of seismic-wave propagation have been widely used in many scientific and engineering fields, e.g., computational rock physics (Saenger and Shapiro, 2002; Quintal et al., 2012; Takekawa et al., 2014a), scattering analysis of seismic waves (Okamoto et al. [2013], for example), triggering effect of seismic waves on an eruption (Lupi et al., 2013), estimations of strong ground motion induced by earthquakes (Graves, 1996; Aochi et al., 2013), etc. In many cases, finite-difference methods (FDMs) or finite-element methods (FEMs) have been used. In FDMs, the use of staggered grids has been developed and contributed to the improvement of the accuracy (Madariaga, 1976; Virieux, 1986) without substantial increase of the computational costs. Then, Saenger et al. (2000) developed the use of rotated staggered grids (FDM-RSGs), and traction-free boundary conditions could become implicitly fulfilled with elastic parameters distributed in the midst of the grids (Bohlen and Saenger, 2006). These approaches are simple and flexible compared to the other explicit implementations. Koketsu et al. (2004) develop a voxel FEM for introducing arbitrary topography and generating a mesh structure faster than methods using the popular tetrahedral mesh. It is also simple to introduce surface topography in the voxel FEM because FEM solutions satisfy the free-surface condition directly. These techniques have provided accurate and fast computations of the seismic-wave propagation including arbitrary topography. Mercerat et al. (2006) apply a spectral element method to reproduce a strong Rayleigh wave, a direct P-wave, converted waves in a model with arbitrary topography and internal material interfaces. Klin et al. (2010) use a pseudospectral method for the numerical computation of the seismic waves in realistic 3D geo-models. In their method, irregular topography is approximated by a staircase of cubic cells. On the other hand, Kumagai et al. (2011) apply an elastic lattice method (ELM) (Toomey and Bean, 2000; O'Brien and Bean, 2004) for simulating seismic wavefields in heterogeneous media with topography. Numerical methods dealing with the arbitrary-shaped free surface with as much accuracy as possible are necessary in the application of seismic-wave propagation.

Recently, Takekawa et al. (2012) proposed a Hamiltonian particle method (HPM) to calculate the strong ground motion induced by earthquakes. Subsequently, Takekawa et al. (2014b) developed a

Manuscript received by the Editor 9 January 2014; revised manuscript received 22 March 2014; published online 16 May 2014.
[1]Kyoto University, Department of Civil and Earth Resources Engineering, Kyoto, Japan. E-mail: takekawa@tansa.kumst.kyoto-u.ac.jp; mikada@gakushikai.jp; goto.tadanori.8a@kyoto-u.ac.jp.

staggered particle technique for HPM to improve the numerical accuracy. In their methods, free surfaces are introduced after removing or ignoring any particles above the surfaces.

In HPM, arbitrary-shaped free surfaces are also dealt with similarly to formally proposed schemes such as FDM-RSG, ELM, etc., in a simple manner. It is important to control the numerical error of HPM for models including arbitrary-shaped free surfaces for applying HPM to seismic-wave propagation. In general, the dispersion analysis for a plane wave propagating through an infinite medium is not sufficient for assessing the numerical error for dealing with Rayleigh waves propagating along irregular free surfaces. This error is induced by the spurious diffractions due to the stair-shaped grid structures and the scattering of Rayleigh waves at small steps. Hayashi et al. (2001) perform several numerical tests of FDM with an irregular free-surface condition and investigate the required number of grid points per wavelength. Bohlen and Saenger (2006) conduct an accuracy analysis of FDM-RSG for simulating Rayleigh waves along dipping planar slopes. Their analysis shows that the RSG can simulate Rayleigh-wave propagation with higher accuracy than the standard staggered grid. Tarrass et al. (2011) develop a new curvilinear scheme for modeling elastic wave propagation in the presence of topography, and they perform a theoretical stability and dispersion analysis of their scheme. Zeng et al. (2012) improve vacuum formulation for arbitrary free surfaces, and they compare their results to those from a spectral element method using homogeneous and heterogeneous models including topography. In this way, the numerical error of such methods for models including arbitrary-shaped free surfaces has to be well understood. However, the obvious accuracy of HPM including surface topography has not been well investigated yet. Because the features of HPM could allow us to efficiently predict not only seismic-wave propagation in earth models but also other applications such as in rock physical problems (e.g., Saenger and Shapiro, 2002), it is important to understand the numerical error of HPM caused by irregular free surfaces for obtaining adequate numerical solutions.

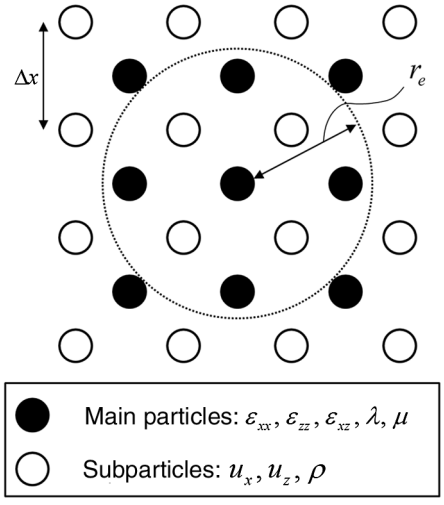

Figure 1. Variable locations of HPM with staggered particles: $u_i(i = x, z)$ and $\varepsilon_{ij}(i, j = x, z)$ are the displacement vector and the strain tensor, respectively; λ, μ are the Lame's constants; and ρ is the density. The displacement vector is defined at the subparticles. On the other hand, the strain tensor is defined at the main particles. The dotted circle represents the influence domain. The main particle at the center has four subparticles inside its influence domain with radius r_e.

In this study, we conduct an accuracy analysis of HPM using models, one with a dipping planar slope and the other with a fold shape hill, to establish a relationship between the desired accuracy and the spatial resolution. We first simulate Rayleigh waves propagating along a horizontal planar free surface. Second, we employ dipping planar slope models, which have different dips of a free surface with respect to the regular alignment of particles, to investigate the accuracy of HPM in comparison with the analytical solution from the Cagniard-de Hoop method. Finally, we simulate a seismic shot gather for the model with a hill to see the accuracy of the method in comparison to the numerical solution from FEM and to demonstrate the effectiveness of HPM.

METHOD

In the present section, we mention only the basic concept of HPM with the staggered particles for simulating seismic waves. Dispersion properties of HPM with staggered particles for a plane wave are shown in Takekawa et al. (2014b). Figure 1 shows the arrangement of main and subparticles. The variable locations of HPM with staggered particles are similar to those of FDM-RSG. The unique approach of HPM is a mesh-free concept of the theory. The deformation gradient tensor at the main particles can be calculated by minimizing the error function as follows:

$$e_i = \sum_j |\mathbf{F}_i \mathbf{r}_{ij}^0 - \mathbf{r}_{ij}|^2 w_{ij}, \tag{1}$$

where e_i is the error function to be minimized; $\mathbf{F}_i$ is the deformation gradient tensor at the main particle i; $\mathbf{r}_{ij}^0$ and $\mathbf{r}_{ij}$ are the initial and current position of subparticle j relative to main particle i, respectively; and w_{ij} is the weighting function. In continuum dynamics, the deformation gradient tensor $\mathbf{F}$ is defined as follows:

$$d\mathbf{x} = \mathbf{F} \cdot d\mathbf{X}, \tag{2}$$

where $d\mathbf{X}$ and $d\mathbf{x}$ are minute vectors in a continuum before and after deformation, respectively (Figure 2). Then, equation 1 means that the deformation gradient tensor at main particle i is estimated by a weighted least-squares method.

We define the weight function as follows:

$$w_{ij} = \begin{cases} r_e/|\mathbf{r}_{ij}| - 1 & (|\mathbf{r}_{ij}| \le r_e) \\ 0 & (|\mathbf{r}_{ij}| > r_e) \end{cases}, \tag{3}$$

where r_e is the radius of the influence domain. The summation of equation 1 is calculated over the particles inside the influence domain. The interactions between particles are controlled by the influence domain. We can obtain the deformation gradient tensor as follows:

$$\begin{aligned} \partial e_i/\partial \mathbf{F}_i &= 2\sum_j (\mathbf{F}_i \mathbf{r}_{ij}^0 - \mathbf{r}_{ij}) \otimes \mathbf{r}_{ij}^0 w_{ij} \\ &= 2\mathbf{F}_i \sum_j \mathbf{r}_{ij}^0 \otimes \mathbf{r}_{ij}^0 w_{ij} - 2\sum_j \mathbf{r}_{ij} \otimes \mathbf{r}_{ij}^0 w_{ij} \\ &= \mathbf{0}, \end{aligned} \tag{4}$$

where

$$\mathbf{F}_i = \sum_j \mathbf{r}_{ij} \otimes \mathbf{r}^0_{ij} w_{ij} \mathbf{A}_i^{-1}, \tag{5}$$

$$\mathbf{A}_i = \sum_j \mathbf{r}^0_{ij} \otimes \mathbf{r}^0_{ij} w_{ij}, \tag{6}$$

where $\mathbf{a} \otimes \mathbf{b}$ means the tensor product of vectors $\mathbf{a}$ and $\mathbf{b}$. The strain tensor, stress tensor, and the total elastic strain energy V can be calculated as follows:

$$\mathbf{E}_i = (\mathbf{F}_i^T \mathbf{F}_i - \mathbf{I})/2, \tag{7}$$

$$\mathbf{S}_i = 2\mu \mathbf{E}_i + \lambda \mathrm{tr}(\mathbf{E}_i)\mathbf{I}, \tag{8}$$

$$V = \sum_i (\mathbf{S}_i : \mathbf{E}_i \Delta B_i)/2, \tag{9}$$

where $\mathbf{E}_i$ and $\mathbf{S}_i$ are the strain and stress tensors at the main particle i, ΔB_i is the volume of the main particle i, $\mathrm{tr}(\mathbf{E})$ is the trace of tensor $\mathbf{E}$, and $\mathbf{S}$:$\mathbf{E}$ is the scalar product of tensors $\mathbf{S}$ and $\mathbf{E}$.

Using the Hamiltonian equation, we can obtain the equation of motion for each subparticle j:

$$\begin{aligned} \Delta m_j \partial \mathbf{v}_j / \partial t &= \partial V / \partial \mathbf{r}_j \\ &= \sum_i (\mathbf{F}_i \mathbf{S}_i \mathbf{A}_i^{-1} \mathbf{r}^0_{\mathrm{ij}} \Delta B_i w_{\mathrm{ij}}), \end{aligned} \tag{10}$$

where Δm_j is the mass of subparticle j. We adopt a symplectic Euler scheme to equation 10 for updating the position vectors. Figure 3 shows a flowchart of the calculation process of the HPM.

The influence domain is one of the key factors to control the numerical accuracy. Takekawa et al. (2012) indicate that a smaller influence domain (compact support) provides better accuracy than a larger one. However, it could be that the number of connecting particles is only one if an inclined slope is discretized in a staircase pattern. Figure 4 shows the staggered particle arrangement near the dipping free surface. Main particles above the free surface are removed. In Figure 4, the subparticle indicated by an arrow has only one connecting main particle if we adopt a compact support. Therefore, we set a larger influence domain to subparticles at the corners of the steps to avoid this situation. We note that this can be implemented in a simple manner owing to the mesh-free concept of the HPM. For subparticles located internally in the model, the compact support is adopted as shown in Figure 1. The effect of the radius of the influence domain will be investigated in Appendix A.

NUMERICAL RESULTS

Horizontal planar surface model

A classic Lamb's problem is used to measure the precision of the HPM in the propagation of seismic waves (Figure 5). A free surface is aligned with the regular latticed arrangement of particles. The traction-free boundary condition can be implemented by ignoring the influence of the outer surrounding particles in the HPM (Suzuki et al., 2007, Takekawa et al., 2014a). The model is set into a 2D isotropic elastic medium with a P-wave velocity of 3454 m/s, an S-wave velocity of 1846 m/s, and a mass density of 2200 kg/m^3. A vertical force is applied to the model. The applied waveform is a Ricker wavelet with a central frequency of 40 Hz. The particle spacing Δx is 0.75 m, and the time step is 5×10^{-5} s.

The numerical waveforms are compared with an analytical solution given by the method of Cagniard-de Hoop. To quantify the relative difference between HPM seismograms and the analytical solution, we define the misfit as follows:

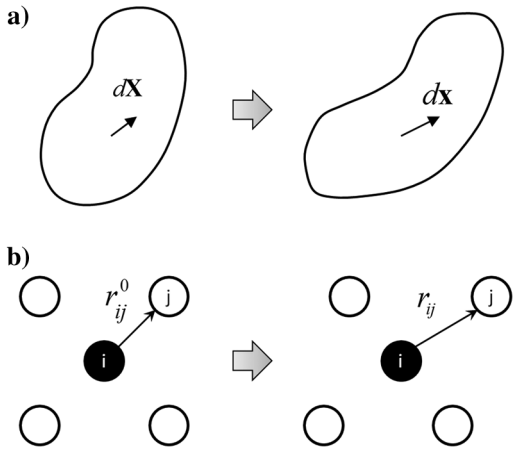

Figure 2. Explanation of physical meanings of the deformation gradient tensor: (a) a schematic figure of the deformation of a continuum and (b) change of the relative position associated with translation of particles.

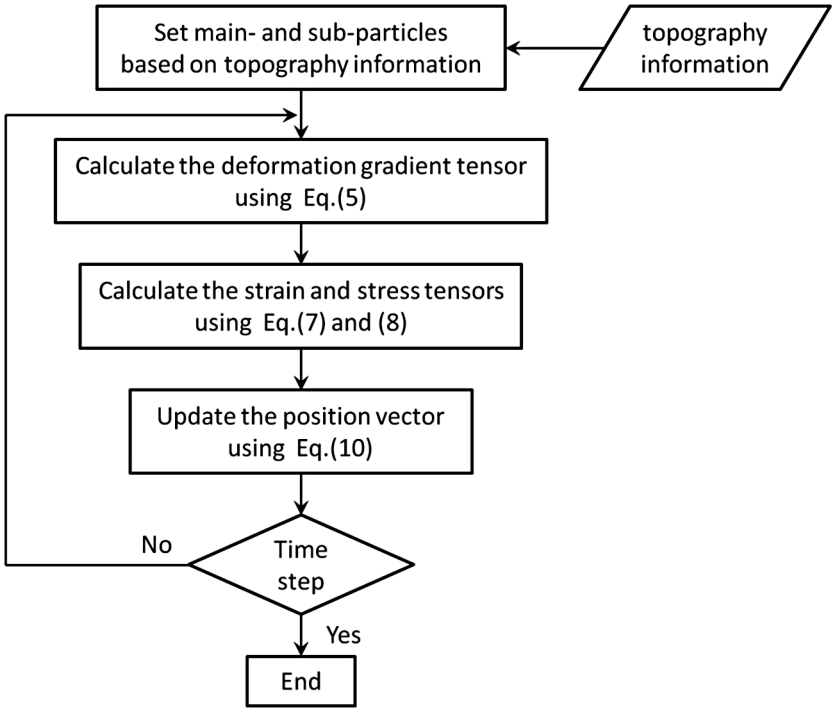

Figure 3. Flowchart of the process of algorithm implementation.

$$\text{misfit} = \frac{\sum_t (S^{\text{NUM}}(t) - S^{\text{ANA}}(t))^2}{\sum_t (S^{\text{ANA}}(t))^2}, \qquad (11)$$

where $S^{\text{NUM}}(t)$ and $S^{\text{ANA}}(t)$ are the numerical and analytical seismograms, respectively. The misfit is calculated over the whole seismogram. In general, a desired accuracy for forward modeling depends on individual problems. It should be determined with respect to each problem. In the present study, we define the desired accuracy as a misfit $\leq$10%.

Figure 6 shows the vertical component of the displacement at the four receivers with the misfits. The solid gray and dashed black lines are analytical and numerical seismograms, respectively. Filled circles at the right side of each seismogram represent the misfits calculated by equation 11. Numerical results are in good agreement with the analytical solutions. In this model, the number of particles in a minimum wavelength is about 20 and the farthest receiver is located at approximately 20 times the minimum wavelength. The misfit at the farthest receiver achieves the desired accuracy. This result indicates that less than 20 particles in a minimum wavelength is sufficient to obtain good accuracy for flat surface models.

Dipping planar slope models

We next calculate seismic-wave propagation along a dipping planar slope. A free surface in this section is introduced by removing particles above the free surface as shown in Figure 4. We change the dipping angle θ of the slope from 0° to 90°. In this section, we use only the farthest receiver whose offset distance is 300 m. The depths of the source and receiver are 4.5 m. So, we can use the same analytical seismogram by rotating the loading direction and the recording component becoming perpendicular to the orientation of the slope. The particle spacing Δx and the time step are the same as the previous ones.

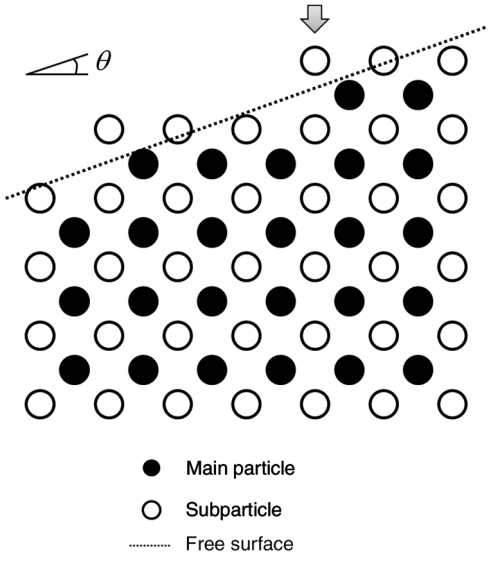

Figure 4. Introduction of a dipping planar free surface. Particles above the free surface are removed. Open and filled circles are the main and subparticles, respectively. The dashed line represents the free surface.

Figure 7 shows the numerical seismograms of the vertical component for different dipping angles. We show the Rayleigh wave event only. The misfit is nearly symmetric around 45°. The misfits increase drastically for dipping angles away from 0° and 90°. However, the misfit decreases near the dipping angle around 45°.

Here, we discuss the reason for the small misfit at 45°. Fuyuki and Matsumoto (1980) indicate that the scattering of Rayleigh waves could be substantial from relatively small steps compared to the wavelength. We therefore check the wavefield around the free surface for 30° and 45°. Figure 8 shows the displacement field

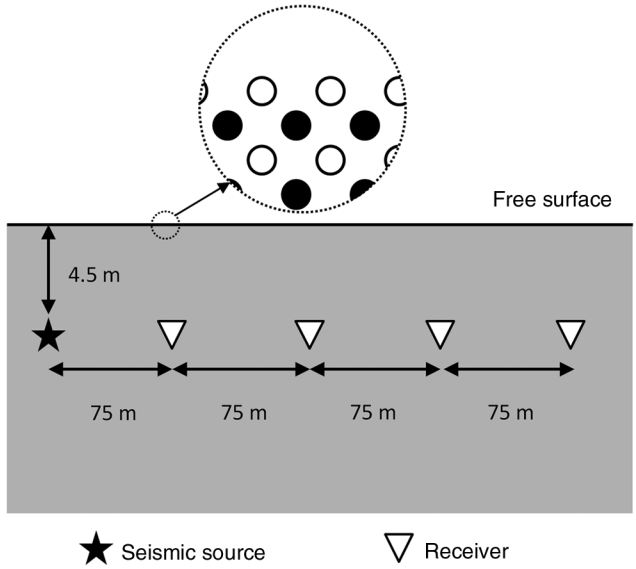

Figure 5. Geometry of the horizontal planar surface model. The seismic source and receivers are buried at a depth of 4.5 m. Four receivers are used with a constant offset of 75 m. Inside the dotted circle is shown the arrangement of the main and subparticles around the free surface.

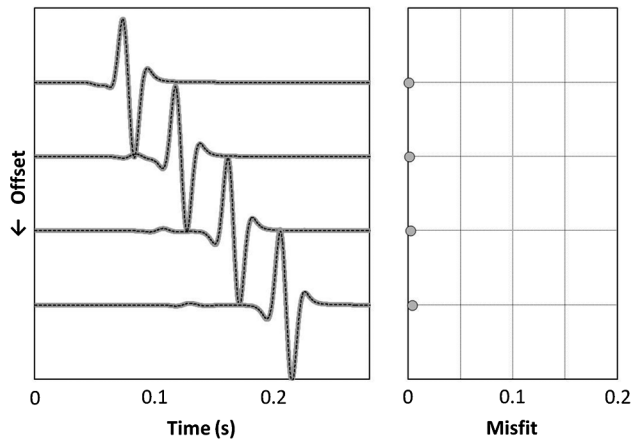

Figure 6. The seismograms of the vertical displacement for different offset distance. The solid gray and dashed black lines are analytical and numerical seismograms, respectively. The misfits calculated by equation 11 are also shown as filled circles on the right.

perpendicular to the inclined free surface after 0.15 s. An arrow indicates the propagation direction of the surface wave. The contour scale is overaccentuated to visualize small-amplitude scattering waves. In Figure 8a, scattered waves with small amplitude behind the surface wave can be observed. In Figure 8b, on the other hand, the scattering waves are not visible because the dipping angle of 45° does not include the steps that generate the scattering waves. This is the reason that the misfit is very small at 45°. A similar trend was also reported in a previous study (Bohlen and Saenger, 2006).

We also calculate the surface wave propagation using FDM-RSG to compare the misfit with that from the HPM. In FDM-RSG, the material properties of the grid points above the free surface are assigned the values of vacuum (i.e., $V_P = V_S = 0$ m/s, $\rho = 0.00125$ kg/m^3). This approach allows us to implement arbitrary-shaped free surfaces without explicitly accounting for them. We use the second-order spatial operator to avoid a reduction in accuracy. Figure 9 shows the numerical seismograms of the vertical component calculated by FDM-RSG. Compared to Figure 7, the misfit at 0° and 90° is slightly smaller than those from the HPM. This means that FDM-RSG has an advantage over the HPM if surface topography is not considered. However, for dipping angles away from 0° and 90°, the misfit increases significantly, although the overall trend is similar to the result from the HPM. This indi-

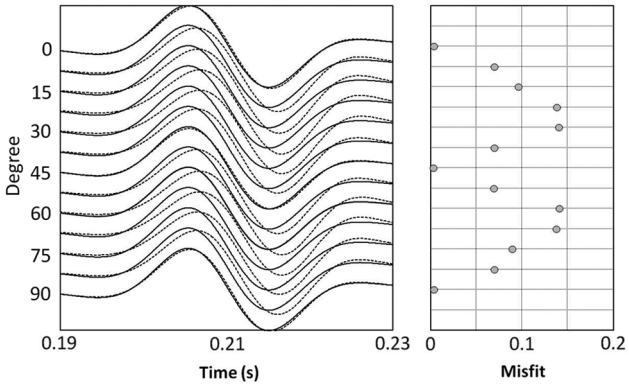

Figure 7. The seismograms of the vertical displacement for different dipping angles with misfits. The particle spacing Δx is 0.75 m. The solid and dashed lines are analytical and numerical seismograms, respectively. The misfits calculated by equation 11 are also shown as filled circles to the right.

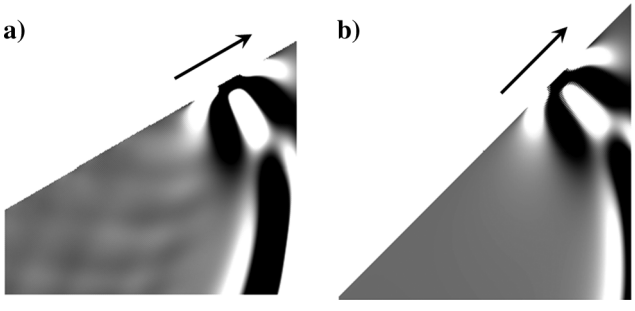

Figure 8. The snapshots of the displacement field perpendicular to the free surface for (a) 30° and (b) 45°. Arrows indicate the propagating direction of the surface wave.

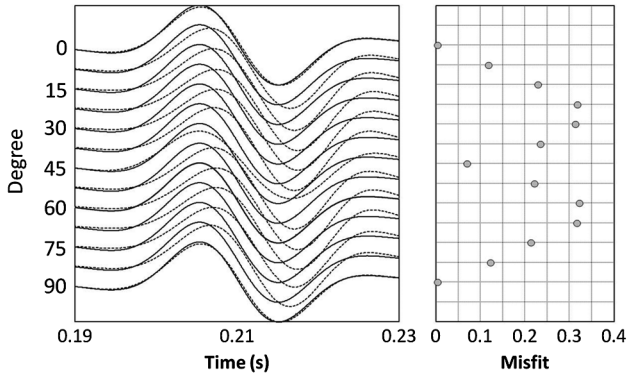

Figure 9. The seismograms of the vertical displacement for different dipping angles with misfits calculated by FDM-RSG. The details are the same as in Figure 7.

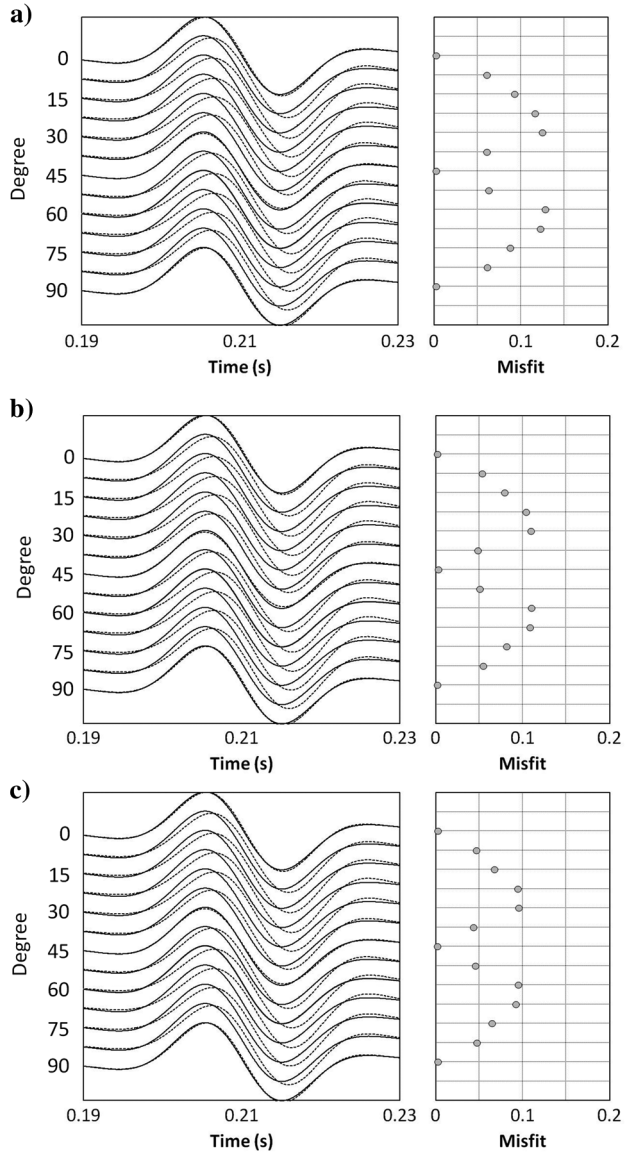

Figure 10. The seismograms of the vertical displacement for different particle spacing with misfits. The particle spacing Δx is (a) 0.72, (b) 0.69, and (c) 0.66 m. The details are the same as in Figure 7.

cates that the HPM requires a lower number of particles for achieving similar accuracy than FDM-RSG.

To investigate the appropriate number of particles in a minimum wavelength for achieving the desired accuracy, we calculate the numerical waveforms with different particle spacing Δx. We refine the spatial resolution ranging from 0.75 to 0.66 m. Figure 10 shows the numerical seismograms and misfits. The misfit decreases gradually as the particle spacing decreases. For particle spacing of 0.66 m, the misfits for all dipping angles achieve the desired accuracy (misfit $\leq 10\%$). The appropriate number of particles in a minimum wavelength for achieving the desired accuracy is between 23 ($\Delta x = 0.66$ m) and 22 ($\Delta x = 0.69$ m). Although the appropriate number depends on the desired accuracy and propagation distance, it could provide an indication of the determination of the spatial resolution.

Hill model

We finally demonstrate the efficiency of the HPM with the staggered particles using an anticlinal layered model whose surface forms a sinusoidal hill as shown in Figure 11a. The geometric configuration of the hill is a single wavelength of the trigonometric function. This model will generate not only a surface wave but also reflected and refracted waves, which are important in explorations of oil and gas reservoirs. The steepest angle at the hillside of the hill is about 45°. We set three receivers at the top, hillside, and foot of the hill. The receivers are located on the free surface. The depth of the seismic source is 4.2 m. The distance between the source and the hill foot is 42 m. The vertical force is applied at the source position. The source function is a Ricker wavelet with a central frequency of 40 Hz. The surface layer has a P-wave velocity of 3122 m/s, an S-wave velocity of 1500 m/s, and a mass density of 2000 kg/m^3. The lower layer, on the other hand, has a P-wave velocity of 4082 m/s, an S-wave velocity of 2500 m/s, and a mass density of 2500 kg/m^3. In this case, the propagation distance of the Rayleigh wave from the source to the receivers A, B, and C is about 20, 28, and 35 minimum wavelengths distance, respectively. We set the particle spacing and the time step to 0.42 m and 5×10^{-5} s, respectively. According to the accuracy test in the previous section, this numerical condition is expected to provide sufficient accuracy at the receiver A whereas the accuracy at the receivers B and C would suffer from the numerical dispersion due to the long-distance propagation.

Figure 11b–11f shows the snapshots of the displacement in the vertical direction after 0.1, 0.15, 0.2, 0.25, and 0.3 s. The surface wave runs up and down the hill, and the waves are reproduced smoothly near the free surface. The reflected and refracted waves are generated when the seismic waves reach the boundary. Trapped waves in the surface layer can also be observed.

Figure 12 shows a single-shot record observed at the free surface. The horizontal and vertical axes are offset distance and two-way traveltime. Many events form complex phases due to multiply reflected waves. The interpretations of main events are identified by dotted lines in the bottom figure. The direct S-wave and surface wave arrive almost at the same time as far as the hilltop. At the other side of the hill, events of these two waves separate from each other because of the difference of the propagation path.

Because it is difficult to calculate analytical solutions for models including arbitrary topography, we use FEM to make reference solutions. FEM can discretize models including arbitrary free surfaces accurately by creating adaptive numerical meshes.

Figure 13 shows the displacement seismograms in the vertical direction at the three receivers A, B, and C. The solid gray and dotted black lines are the results from FEM and HPM, respectively. At the hilltop (receiver A), a large amplitude can be observed because of the simultaneous arrival of the direct S-wave and surface wave. At receivers B and C, these two phases separate from each other. Our numerical seismograms are in good agreement with those from FEM, although relatively high error can be observed in part of the surface wave. The misfits between HPM and FEM are 3.3%,

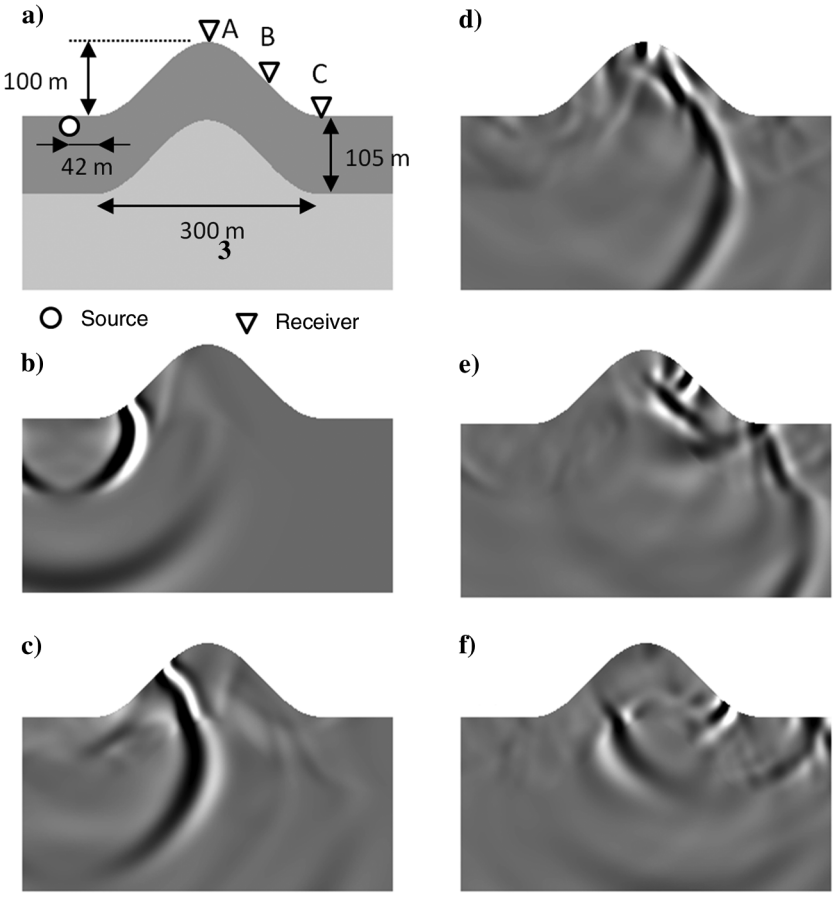

Figure 11. A schematic figure of a layer model with a hill (a) and the snapshots of the vertical displacement field after (b) 0.1, (c) 0.15, (d) 0.2, (e) 0.25, and (f) 0.3 s. The seismic source is buried at a depth of 4.2 m near the hill foot. Three receivers are set on the free surface.

5.6%, and 10.9% at receivers A, B, and C, respectively. The relatively high misfit at receiver C is mainly induced by the delay of the arrival of the surface wave indicated by a broken circle. This is caused by the long propagation distance between the seismic source and the receiver C. The large misfit of receiver C meets our expectation based on the accuracy analysis in the previous section.

CONCLUSION

HPM with staggered particles is a class of mesh-free numerical methods. Because it is simple to introduce the traction-free boundary condition in the HPM, the accuracy of the HPM for models including irregular topography is investigated in this study using the staggered particles in the simulation of seismic-wave propagation along planar free surfaces. The numerical accuracy suffers from the dipping planar free surfaces, whereas the 45° slope provides good accuracy. We compared the result with that from FDM-RSG. The accuracy of FDM-RSG was slightly higher than the HPM if the free surface was flat. However, for the dipping free surfaces, the HPM showed better agreement with the analytical solutions than FDM-RSG.

Next, we investigated the required number of particles in a minimum wavelength for achieving the desired accuracy, which was defined as misfit $\leq$10% in the present study. Approximately 23 particles in a minimum wavelength are needed to achieve sufficient accuracy (misfit $\leq$10%) for all dipping angles. For the simulation of Rayleigh wave propagation for more than 20 minimum wavelengths distance, a larger number of particles would be required. Although the desired accuracy would depend on individual problems, these relationships among the spatial resolution, propagation distance, and numerical accuracy could help to determine the spatial resolution for arbitrary models including topography.

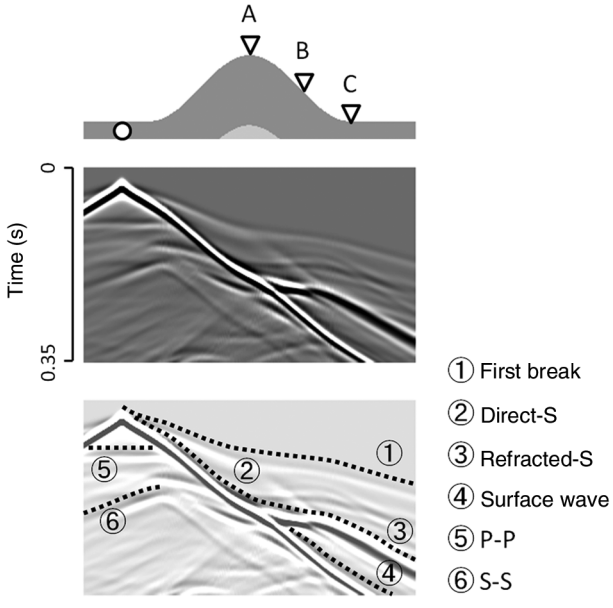

Figure 12. A single-shot record at the free surface. The dotted lines in the bottom figure indicate main events in the record.

We finally used a layered model with a hill to demonstrate the effectiveness of the HPM for simulating not only Rayleigh wave propagation along an arbitrary topography but also reflected and refracted waves. We compared the waveforms calculated by HPM with those from FEM. Our numerical results are in good agreement with those from FEM.

Our results indicate that HPM with staggered particles could be one of the solutions to simulate seismic waves including irregular topography. The strong point of HPM is the simplicity of introducing free surfaces. There is no need for creating an adaptive mesh structure like FEM. This would lead to a reduction of time for preprocessing. On the grounds of the feature described above, applications of HPM are expected for not only the simulations of surface waves but also computational rock experiments and seismic scattering analyses including fractures.

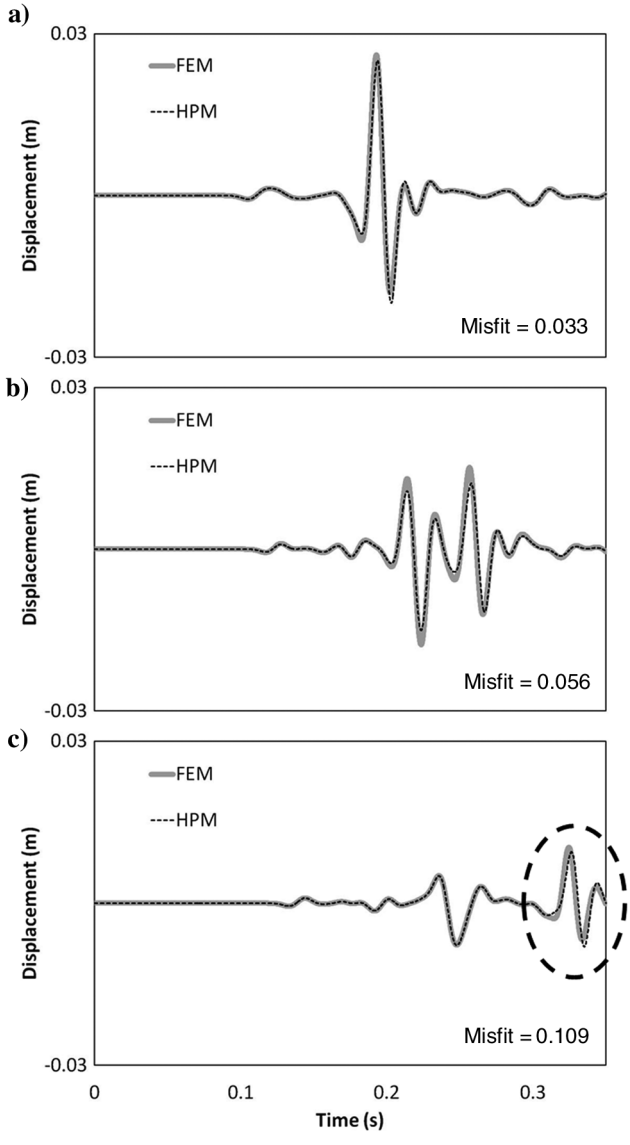

Figure 13. Seismograms of the vertical displacement at receivers A, B, and C. The solid gray and dashed black lines are seismograms from FEM and HPM, respectively. The misfits between FEM and HPM are shown at the lower right corner of each seismogram.

ACKNOWLEDGMENTS

This work was supported by MEXT/JSPS KAKENHI grant no. 24760361. We thank the editor and two anonymous reviewers for their valuable comments that improved the paper.

APPENDIX A

EFFECT OF THE INFLUENCE DOMAIN

In HPM, the numerical accuracy is affected by the radius of the influence domain. Here, we test the effect of the radius on the numerical accuracy. We double the radius of the influence domain as shown in Figure A-1. In this case, the number of particles inside the influence domain increases from 4 to 12. We calculate the surface-wave propagation using the flat surface model shown in Figure 5. Figure A-2 shows the vertical component of the displacement at the four receivers with the misfits. Compared with Figure 6, the misfits increase significantly. This trend corresponds with the previous study (Takekawa et al., 2012); i.e., a larger support of the influence domain increases the misfit. In FDM, higher-order schemes (e.g., Levander, 1988) can be achieved by determining the coefficients of the operator to make it cancel out higher order error terms. The HPM, however, does not take the cancellation of the error terms into consideration if the number of particles inside the influence domain increases. The accuracy of the HPM depends on the linearity of the deformation inside the influence domain (equation 1). This means that the increment of the number of particles works against the improvement of the numerical accuracy because the linearity of the deformation inside the influence domain is not held.

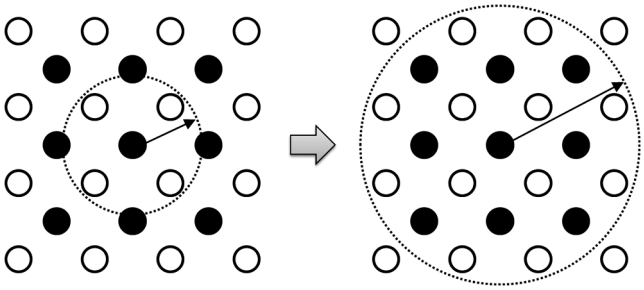

Figure A-1. Change of the influence domain.

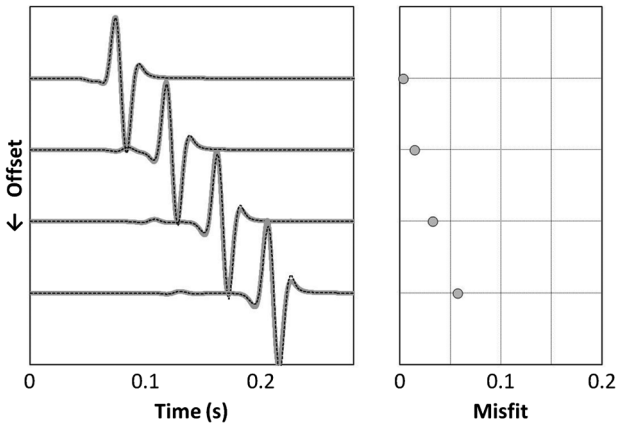

Figure A-2. The seismograms of the vertical displacement for different offset distances. The details are the same as in Figure 6.

REFERENCES

Aochi, H., A. Ducellier, F. Dupros, M. Delatre, T. Ulrich, F. Martin, and M. Yoshimi, 2013, Finite difference simulations of seismic wave propagation for the 2007 Mw 6.6 Niigata-ken Chuetsu-oki earthquake: Validity of models and reliable input ground motion in the near-field: Pure and Applied Geophysics, **170**, 43–64, doi: 10.1007/s00024-011-0429-5.

Bohlen, T., and E. H. Saenger, 2006, Accuracy of heterogeneous staggered-grid finite-difference modeling of Rayleigh waves: Geophysics, **71**, no. 4, T109–T115, doi: 10.1190/1.2213051.

Fuyuki, M., and Y. Matsumoto, 1980, Finite-difference analysis of Rayleigh wave scattering at a trench: Bulletin of the Seismological Society of America, **70**, 2051–2069.

Graves, R. W., 1996, Simulating seismic wave propagation in 3D elastic media using staggered-grid finite differences: Bulletin of the Seismological Society of America, **86**, 1091–1106.

Hayashi, K., D. R. Burns, and M. N. Toksoz, 2001, Discontinuous-grid finite-difference seismic modeling including surface topography: Bulletin of the Seismological Society of America, **91**, 1750–1764, doi: 10.1785/0120000024.

Klin, P., E. Priolo, and G. Seriani, 2010, Numerical simulation of seismic wave propagation in realistic 3-D geo-models with a Fourier pseudo-spectral method: Geophysical Journal International, **183**, 905–922, doi: 10.1111/j.1365-246X.2010.04763.x.

Koketsu, K., H. Fujiwara, and Y. Ikegami, 2004, Finite-element simulation of seismic ground motion with a voxel mesh: Pure and Applied Geophysics, **161**, 2183–2198, doi: 10.1007/s00024-004-2557-7.

Kumagai, H., T. Saito, G. O'Brien, and T. Yamashina, 2011, Characterization of scattered seismic wavefields simulated in heterogeneous media with topography: Journal of Geophysical Research, **116**, B03308, doi: 10.1029/2010JB007718.

Levander, A. R., 1988, Fourth-order finite-difference P-SV seismograms: Geophysics, **53**, 1425–1436, doi: 10.1190/1.1442422.

Lupi, M., E. H. Saenger, F. Fuchs, and S. A. Miller, 2013, Lusi mud eruption triggered by geometric focusing of seismic waves: Nature Geoscience, **6**, 642–646, doi: 10.1038/ngeo1884.

Madariaga, R., 1976, Dynamics of an expanding circular fault: Bulletin of the Seismological Society of America, **66**, 639–666.

Mercerat, E. D., J. P. Vilotte, and F. J. Sanchez-Sesma, 2006, Triangular spectral element simulation of two-dimensional elastic wave propagation using unstructured triangular grids: Geophysical Journal International, **166**, 679–698, doi: 10.1111/j.1365-246X.2006.03006.x.

O'Brien, G., and C. Bean, 2004, A 3D discrete numerical elastic lattice method for seismic propagation in heterogeneous media with topography: Geophysical Research Letters, **31**, L14608, doi: 10.1029/2004GL020069.

Okamoto, K., H. Mikada, T. Goto, and J. Takekawa, 2013, Numerical analysis of the relationship between time-variant coda-Q and the variation in crustal stress: Geophysical Journal International, **195**, 575–581, doi: 10.1093/gji/ggt243.

Quintal, B., H. Steeb, M. Frehner, S. M. Schmalholz, and E. H. Saenger, 2012, Pore fluid effects on S-wave attenuation caused by wave-induced fluid flow: Geophysics, **77**, no. 3, L13–L23, doi: 10.1190/geo2011-0233.1.

Saenger, E. H., N. Gold, and S. A. Shapiro, 2000, Modeling the propagation of elastic waves using a modified finite-difference grid: Wave Motion, **31**, 77–92, doi: 10.1016/S0165-2125(99)00023-2.

Saenger, E. H., and S. A. Shapiro, 2002, Effective velocities in fractured media: A numerical study using the rotated staggered finite-difference grid: Geophysical Prospecting, **50**, 183–194, doi: 10.1046/j.1365-2478.2002.00309.x.

Suzuki, Y., S. Koshizuka, and Y. Oka, 2007, Hamiltonian moving-particle semi-implicit (HMPS) method for incompressible fluid flows: Computer Methods in Applied Mechanics and Engineering, **196**, 2876–2894, doi: 10.1016/j.cma.2006.12.006.

Takekawa, J., R. Madariaga, H. Mikada, and T. Goto, 2012, Numerical simulation of seismic wave propagation produced by earthquake by using a particle method: Geophysical Journal International, **191**, 1305–1316. doi: 10.1111/j.1365-246X.2012.05676.x.

Takekawa, J., H. Mikada, and T. Goto, 2014a, Numerical simulation using a Hamiltonian particle method for effective elastic properties in cracked media: Exploration Geophysics, doi: 10.1071/EG13098.

Takekawa, J., H. Mikada, and T. Goto, 2014b, A Hamiltonian particle method with a staggered particle technique for simulating seismic wave

propagation: Pure and Applied Geophysics, doi: 10.1007/s00024-013-0763-x.

Tarrass, I., L. Giraud, and P. Thore, 2011, New curvilinear scheme for elastic wave propagation in presence of curved topography: Geophysical Prospecting, **59**, 889–906, doi: 10.1111/j.1365-2478.2011.00972.x.

Toomey, A., and C. J. Bean, 2000, Numerical simulation of seismic waves using a discrete particle scheme: Geophysical Journal International, **141**, 595–604, doi: 10.1046/j.1365-246x.2000.00094.x.

Virieux, J., 1986, P-SV wave propagation in heterogeneous media: Velocity-stress finite difference method: Geophysics, **51**, 889–901, doi: 10.1190/1.1442147.

Zeng, C., J. Xia, R. D. Miller, and G. P. Tsoflias, 2012, An improved vacuum formulation for 2D finite-difference modeling of Rayleigh waves including surface topography and internal discontinuities: Geophysics, **77**, no. 1, T1–T9, doi: 10.1190/geo2011-0067.1.